Theor Appl Climatol (2014) 116:549–564
DOI 10.1007/s00704-013-0963-4

ORIGINAL PAPER

Role of orography in modulating space–time scales of convection over South Asia

Arindam Chakraborty · Ravi S. Nanjundiah

Received: 19 October 2012 / Accepted: 28 June 2013 / Published online: 31 July 2013

Abstract Propagation of convective systems in the meridional direction during boreal summer is responsible for active and break phases of monsoon over south Asia. This region is unique in the world in its characteristics of monsoon variability and is in close proximity of mountains like the Himalayas. Here, using an atmospheric general circulation model, we try to understand the role of orography in determining spatial and temporal scales of these convective systems. Absence of orography (*noGlOrog*) decreased the simulated seasonal mean precipitation over India by 23 % due to delay in onset by about a month vis-a-vis the full-mountain case. In *noGlOrog*, poleward propagations were absent during the delayed period prior to onset. Post-onset, both simulations had similar patterns of poleward propagations. The spatial and temporal scales of propagating clouds bands were determined using wavelet analysis. These scales were found to be different in full-mountain and no-mountain experiments in June–July. However, after the onset of monsoon in *noGlOrog*, these scales become similar to that with orography. Simulations with two different sets of convection schemes confirmed this result. Further analysis shows that the absence (presence) of meridional propagations during early (late) phase of summer monsoon in *noGlOrog* was associated with weaker (stronger) vertical shear of zonal wind over south Asia. Our study shows that orography plays a major role in determining the time of onset over the Indian region. However, after onset, basic characteristics of propagating convective systems and therefore the monthly precipitation over India, are less sensitive to the presence of orography and are modulated by moist convective processes.

A. Chakraborty (✉) · R. S. Nanjundiah
Centre for Atmospheric and Oceanic Sciences,
Indian Institute of Science,
Bangalore, India
e-mail: arch@caos.iisc.ernet.in

R. S. Nanjundiah
e-mail: ravi@caos.iisc.ernet.in

A. Chakraborty · R. S. Nanjundiah
Divecha Centre for Climate Change, Indian Institute of Science,
Bangalore, India

1 Introduction

Orography plays a major role in determining the location of wet and dry regions on the earth. Presence of mountains modifies the spatial pattern of diabatic heating and atmospheric circulation. In their pioneering study, Hahn and Manabe (1975) used a global model to show that south Asian monsoon weakens in absence of global orography. In subsequent studies, Manabe and Broccoli (1990) and Broccoli and Manabe (1992) had shown that arid climate seen over most of the midlatitude belts are due to the presence of mountains. In their simulation with orography, midlatitude arid climates were well captured. However, when mountains were removed, those regions became more wet. They had concluded that the presence of huge mountains like the Tibetan Plateau and the Rockies generates large amplitude stationary waves which are responsible for this dry climate of midlatitudes.

The importance of Tibetan Plateau as an elevated heat source and its effect on south Asian summer monsoon circulation has been discussed by numerous authors (e.g., Flohn 1957, 1960, 1968; Yeh 1981; Luo and Yanai 1983, 1984; Chen et al. 1985; He et al. 1987; Li and Yanai 1996). The effect of Himalayan orography in the context of paleoclimate has been investigated by Prell and Kutzbach (1992, 1997). An et al. (2001) have studied the effect of phased

uplift of the Himalayas on summer monsoon over south Asia. Their simulations show that rainfall increased only after the upliftment of Western part of Tibet. Using 14-year observed data sets, Li and Yanai (1996) have shown that sensible heating over the Tibetan Plateau during spring leads to a meridional temperature gradient, which is concurrent with the onset of the Asian summer monsoon. Experiments using a coupled general circulation model (GCM) by Kitoh (2004) show that monsoon over east Asia goes through a drastic change when mountain height in the model is set to at least 60 % of the present. A recent study by Boos and Kuang (2010) has shown that although the elevated heating of the Tibetan Plateau affects local precipitation, the primary mechanism by which the Himalayas affects Indian summer monsoon is by mechanically insulating midlatitude cold-dry air from warm-moist air over the subcontinent, confirming the earlier results of Chakraborty et al. (2006).

Slingo et al. (2004) used an atmospheric GCM and European Centre for Medium-Range Weather Forecasts (ECMWF) reanalysis data sets to study the impact of east African highlands on the climate of western Indian Ocean and surrounding areas. Their study indicates that these apparently not-so-high mountains have a large impact in redistributing precipitation pattern over India and east Asia. Moreover, the presence of east African highlands could increase upwelling along west Indian Ocean and thereby cool the ocean surface. Chakraborty et al. (2009) showed that absence of east African highlands can increase monsoon precipitation over Indian region due to stronger wind that enables higher convergence of moisture. It was shown that the low-level jet near the coast of Somalia can exists even without the east African mountains on account of Gill type response due to convective heating over Bay of Bengal.

Chakraborty et al. (2002), using a global GCM had studied the seasonal mean changes in Indian summer monsoon due to absence of global orography. It was shown by Chakraborty et al. (2006) that in absence of orography, atmosphere becomes more stable during early parts of the monsoon (June–July).

That the intensity of boreal monsoon precipitation is determined by active and break spells of monsoon has been shown by many previous studies (Krishnamurthy and Shukla 2007). This, in turn, is related to northward propagation of convective zones over the northern Indian Ocean (Krishnamurti et al. 1976; Sikka and Gadgil 1980). Therefore, it is required to study the spatial and temporal scales of this northward propagation over the Indian longitudes quantitatively and comprehensively. For example, one needs to know how the spatial scales differ during years of good and weak monsoon. Hence, it will be of great interest to study how orography influences the temporal and spatial scales of northward propagation of convection.

Temporal and spatial scales of a propagating waves can be analyzed using fast Fourier transformation (FFT). Many studies used this technique to calculate the time period and wave number of atmospheric waves. Hayashi (1982) and Wheeler and Kiladis (1999) used two-dimensional FFT analysis to study zonally propagating equatorial waves in the atmosphere. This technique decomposes the wave into space and time to obtain time period of oscillation at every spatial wave number. However, since this technique is based on FFT, this cannot be used to study northward propagation of convection over the south Asian region because the spatial scales of these waves are space bounded usually between 10° S to 30° N.

Wavelet analysis is a tool to study time series of data (or a sequence of data in space). This method is relatively recent compared to the traditional tools like the Fourier, Bessel's, Legendre, or maximum entropy, etc.—with the added advantage that localized variation of power can be studied using wavelets (Daubechies 1990). A detailed description of the theory of wavelet analysis can be found, for example, in Daubechies (1992) and in Percival and Walden (2000). The wavelet was used as a tool to analyze geophysical time series by many authors (Weng and Lau 1994; Gu and Philander 1995; Wang and Wang 1996; Gamage and Blumen 1993; Baliunas et al. 1997; Meyers et al. 1993; Liu 1994; Farge 1992; Foufoula-Georgiou and Kumar 1995; Kailas and Narasimha 2000). A practical guide to wavelet analysis in atmospheric and oceanic sciences can be found in Torrence and Compo (1998). The analysis method adopted in this study was originally from Shanker and Nanjundiah (2004).

Recently, Chakraborty and Nanjundiah (2012) have suggested a technique to quantify the spatial and temporal scales of northward propagation of convection over south Asia using Tropical Rainfall Measurement Mission (TRMM) data sets. A new index, termed as the Index for Spatial Extent of Convection (ISEC) was introduced as a measure for the spatial extent of the meridionally propagating convection bands. It was seen that the value of ISEC were high (low) during above (below) normal monsoon years. Moreover, this index varies during active and break phases of monsoon much in the same way as during good and weak monsoon years.

Primary goal of this study is to understand the role of orography in determining these spatial and temporal scales of propagation of convection in the meridional direction. Moreover, we try to understand the role of orography in determining the frequency distribution of daily precipitation over south Asia at various precipitation ranges. We have performed perturbed orography experiments using a GCM for this purpose. The model used is described in Section 2. Section 3 lists the experiments done with the model. The methodology adapted in this study is detailed in Section 4.

Section 5 illustrates the results in detail followed by major conclusions of this study.

2 Model used

We have used the National Centre for Medium-Range Weather Forecasts (NCMRWF) GCM, which is a modified form of the research version of National Meteorological Center (now National Center for Environmental Prediction) global spectral model (Sela 1982, 1988). The model has a triangular truncation at 80 waves, which corresponds to about 1.4° resolution in grid space near the equator. It has 18 vertical sigma levels with more closely spaced levels near the surface and near the tropopause. Simplified Arakawa–Schubert (SAS) scheme (Grell 1993) was used for convection parameterization. We also used the Kuo convection scheme (Anthes 1977) for comparison with the result obtained from the SAS scheme and, therefore, taking care of the possibility of any change due to the cumulus parameterization scheme in the model. This model was previously used for various studies related to convection schemes (Das et al. 2001, 2002) and onset of monsoon (Chakraborty 2002, 2006), among others.

3 Experimental details and data sets

We have performed two sets of experiments. The first is the *control* experiment that used mean orography as obtained in the NCEP/NCAR (National Center for Atmospheric Research) reanalysis data sets. In the second set of experiments, orography was removed from the entire globe. This will be termed as *noGlOrog* in this paper.

Ensemble simulations with five different initial conditions corresponding to 00 GMT of 1–5 March 1998 were performed for both the experiments, and the model was integrated up to 30 September 1998. Initial conditions were created from NCEP/NCAR reanalysis data sets. Surface boundary condition over the ocean were obtained from Reynolds and Smith (1994) monthly mean data sets, and the SST was linearly interpolated to model run time. Output frequency of the model was once daily (mean), and output of first 2 months were not considered for analysis considering it as model spin-up time. It was seen that (not shown) temperature, moisture, and surface pressure of the model get stabilized within this period.

In considering monthly mean results, we have taken mean among the five members of the ensemble. To study intraseasonal oscillations, it was not possible to do ensemble mean of a parameter prior to any analysis since usually ensemble members were out of phase on a daily scale and any averaging between them removes the variability in time and space. Therefore, to study intraseasonal variability, we have used two different approaches. To study time–latitude variations, only one ensemble member corresponding to initial conditions of 00 GMT of 1 March 1998 was used for Hovmoller diagrams (Fig. 4). The broad features of intraseasonal variation were similar across ensemble members.

Further to determine the scales of propagation, wavelet transformation was applied to each of the members separately, and the ensemble mean of the wavelet spectra are shown in this paper.

TRMM 3B42 data sets were used for observational analysis. The time resolution of this data set is 3-hourly, and spatial resolution is $0.25° \times 0.25°$. This data set for the year 1998 was regridded in space and time to the model resolution using area average method that preserves total water content.

4 Methodology

This study uses Morlet wavelet, a complex valued function, which can be written as

$$\psi_0(\eta) = \pi^{-0.25}\, e^{i\omega_0\eta}\, e^{-\eta^2/2} = \sqrt{\frac{2}{\pi}}\, e^{i\omega_0\eta} \quad \frac{1}{\sqrt{2\pi}}\, e^{-\eta^2/2} \tag{1}$$

where the first term is a plain wave and the second term is a Gaussian PDF. We have used a value for ω_0, the non-dimensional frequency, as 6.

Wavelet transform of the time series x_n can be written as the convolution of a scaled and translated version of this wavelet function:

$$W_n(s) = \sum_{n'=0}^{N-1} x_{n'} * \psi^* \left(\frac{(n'-n)\delta t}{s} \right) \tag{2}$$

where the "$*$" implies complex conjugate. It is possible to study the amplitude of a time series at various scales by varying the wavelet scale s and the translation time index n. The convolution of Eq. 2 was done in Fourier space to save computational time. We have calculated Fourier wavelength for a particular scale s using the following relation:

$$\text{Fourier wavelength} = \frac{4\pi s}{\omega_0 + \sqrt{2+\omega_0^2}} \tag{3}$$

Therefore, this Fourier wavelength is very close (1.0330 times) to the wavelet scale for $\omega_0 = 6$.

Two-dimensional wavelet transform was performed on a field $f(x,t)$ which is a function of space (x) and time (t). In doing so, at first, one dimensional transform was

performed over space at every time point to obtain the three-dimensional field $y(s_x, x, t)$:

$$y(s_x, x, t) = f(x, t) * \frac{1}{\sqrt{s_x}} \psi_0 \left(\frac{x}{s_x} \right) \quad (4)$$

where s_x represents the spatial scale. The time average of the above three-dimensional field for the period N_1 to N_2 is:

$$\hat{Y}(s_x, x) = \frac{1}{N_2 - N_1 + 1} \sum_{N_1=1}^{N_2} |y(s_x, x, t)|^2 \quad (5)$$

This represents the spatial scale over that time period.

Next, wavelet transform along time dimension gives the four-dimensional field $w(s_x, x, s_t, t)$:

$$w(s_x, x, s_t, t) = y(s_x, x, t) * \frac{1}{\sqrt{s_t}} \psi_0 \left(\frac{t}{s_t} \right) \quad (6)$$

where s_t represents the time scale.

4.1 Significance testing

We have performed significance testing of the wavelet transformed coefficients against a red noise spectrum based on the assumption that the data are purely univariate lag-1 autoregressive [AR(1) or Markov]:

$$f(x, t) = \alpha f(x - 1, t) + z_n$$
$$s(s_x, x, t) = \beta_s s(s_x, x, t - 1) + z_n$$

where α is the lag-1 correlation coefficient over space domain at a particular time instant, β_s is the lag-1 correlation coefficient in time at a particular location, and z_n is a white noise process. For computational purposes, we have regridded the model data sets to $1^\circ \times 1^\circ$ spatial grid boxes and then applied this methodology. This is consistent with the fact that the speed of northward propagating waves is of the order of 1° per day in latitude. The results are not sensitive to the choice of time-lag (Chakraborty and Nanjundiah 2012).

A chi-square distribution with the following number of degrees of freedom was used to calculate significance level:

$$D.O.F = 2(N_2 - N_1 + 1) \quad (7)$$

The factor 2 arises due to the fact that Morlet wavelet is a complex valued wavelet function that has real and imaginary components and they are normally distributed (Torrence and Compo 1998; Shanker and Nanjundiah 2004). A detailed methodology of the two-dimensional wavelet transform used in this paper is provided in Chakraborty and Nanjundiah (2012) and Shanker and Nanjundiah (2004).

Figure 1a shows a theoretical wave traveling from 10° S to 30° N given by the equation:

$$z = 10 sin 2\pi (x/40 - t/30), \quad (8)$$

where x is in degrees and t is in days. The time period of this wave is 30 days and spatial scale is 40° with amplitude 10. The northward extent of these propagating waves follows an envelope of a sine wave with half wavelength of 122 days (June–September) and amplitude 40°. This envelope mimics the onset and withdrawal phases of Indian summer monsoon and the waves embedded inside are representative of northward propagating convective bands in the intraseasonal time scales. The corresponding wavelet transform is given in Fig. 1b. The cone of influence (COI), beyond which edge effects become important due to the finite length of the data, is shown as thick black line. Note that the highest amplitude of this theoretical transformation is centered at 10° N with a spatial scale of around 40°. This is consistent with the equation of the wave considered here. The second theoretical data were similar to that of the first one but without any intraseasonal oscillation embedded inside the seasonally migrating envelope (Fig. 1c). The difference in spatial scales between these two data sets will show if the intraseasonal oscillation has any effect on the scale of propagation as proposed in the paper. Note that, when the intraseasonal oscillation (ISO) is embedded within the seasonally varying onset-withdrawal envelope, a distinct scale of propagation is seen. However, once the ISO is removed (Fig. 1c), the spatial scale disappears (Fig. 1d). This shows that the dominant spatial scales selected by our algorithm are indeed representative of ISO of convection. The location of the dominant spatial scale does not depend on the choice of the domain. Rather, it is the center of the extent to which the wave propagates. We have studied this using the same theoretical wave but using a different domain size and found that the center of propagation coincides with the location of the dominant spatial scale of transformation (not shown).

5 Results

Figure 2 shows mean precipitation over south Asian region from observational estimates (TRMM) and NCMRWF simulation during the summer months of 1998. The model simulations include the full-orography (control) and no-orography *(noGlOrog)* scenarios both for SAS and Kuo cumulus convection. Ensemble mean precipitation during June–July and August–September were shown separately to distinguish the impact of orography during the first and second half of the season. The averaged precipitation over the Indian region ($70^\circ - 90^\circ$ E, $8^\circ - 28^\circ$ N, land part; region shown as dashed box in Fig. 2a) for all these cases are indicated by numbers at the top-left corner of corresponding panels. This figure shows that the control simulation of the model with SAS convection was able to capture the magnitude and variation of subseasonal precipitation over the Indian region when compared to the TRMM data set.

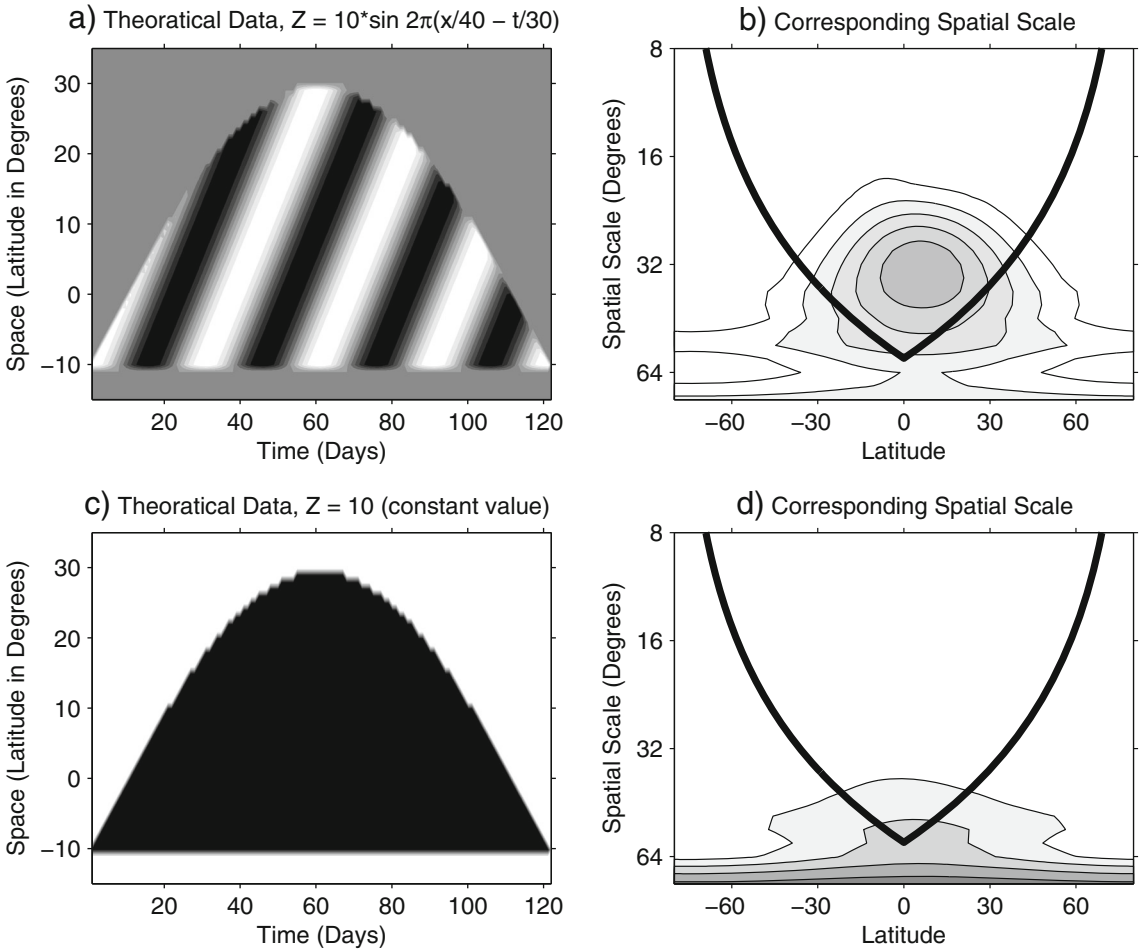

Fig. 1 **a** A theoretical wave with time period 30 days and wavelength 40° traveling between 10° S and 30° N within an envelope of a sine wave representing the onset and withdrawal of Indian monsoon. *Dark area* corresponds to wave activity and *light-shaded regions* correspond to quiescent state. **b** Corresponding Morlet wavelet spectrum showing maximum energy at about 40° spatial scale centered at around 10° N. **c** A theoretical data similar to that (**a**) above but without any intraseasonal oscillation embedded in it. **d** Wavelet spectrum corresponding to data in (**c**)

Control simulation with the Kuo cumulus convection also shows a similar variation of subseasonal precipitation. However, the magnitudes were higher by 2 to 4 mm day^{-1} compared to the observational estimates.

Figure 2g–j show that precipitation over the Indian region during June and July in the *noGlOrog* simulation were reduced by more than 50 % when compared to the control. This is true for both SAS and Kuo cumulus convection. Inside these panels, we have also indicated the significance level (using a *t* test) at which the mean of the *noGlOrog* simulation differs from the corresponding control simulation. This reduction was due to intrusion of midlatitude cold-dry air into the Indian subcontinent that reduced convective available potential energy and increased vertical stability of the atmosphere (Chakraborty et al. 2006). On the other hand, precipitation over the Indian region increased during August–September to 169 % in SAS (145 % in Kuo) when orography was removed all over the globe vis-a-vis its June–July value. Due to this increase, the August–September mean precipitation in *noGlOrog* simulation became comparable to that from the control with SAS convection scheme. However, the mean value during August–September in Kuo simulation without orography was still about 2.5 mm day^{-1} lower than the corresponding control value.

Comparing subpanels f and j of Fig. 2, we find that most of the differences between control and *noGlOrog* simulations during August–September was near the regions of large orography. Kuo scheme is based on large scale mass convergence in the lower troposphere and gives high precipitation over the regions of orographic uplift (compare Fig. 2a, c and d, f). When orography was not present in the model, the forced uplift of moist air near the mountains was missing in the Kuo scheme and, hence, the precipitation reduced substantially compared to its full-mountain simulation. This makes the mean precipitation from *noGlOrog*

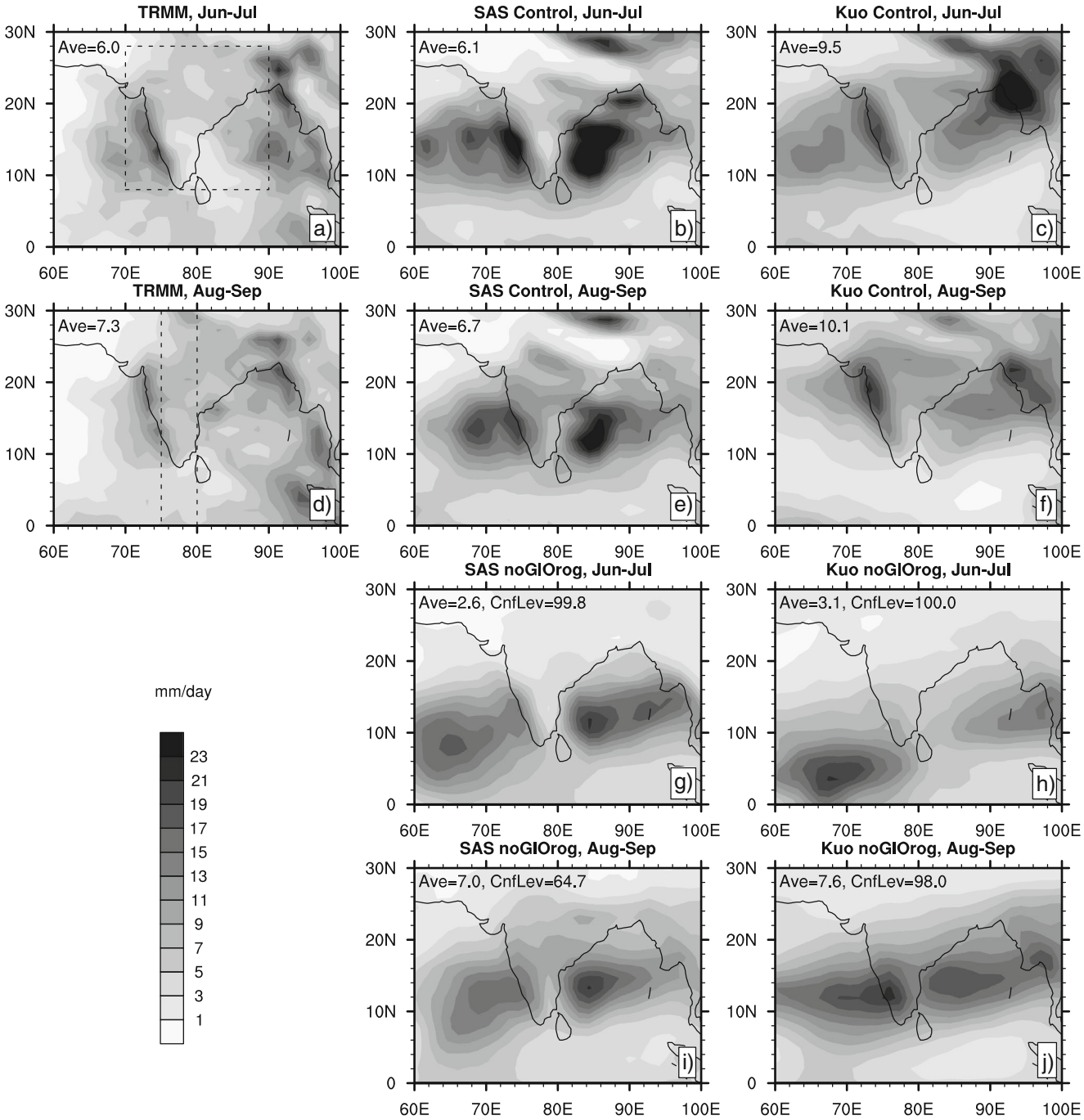

Fig. 2 Precipitation over the south Asian region during June–July and August–September 1998 from TRMM data sets (*left panels*), and model simulation with full (*control*) and no orography *(noGlOrog)* using SAS (*middle panels*) and Kuo (*right panels*) cumulus convection. Area mean precipitation (*only over the land part*) between 70°–90° E, 8°–28° N (shown by dashed box in panel **a**) is indicated by *numbers at the top-left corner* of each panel. The latitude band through the center of the Indian peninsular (75°–80° E), shown by *dashed lines* in panel (**d**), was used for analysis of spatial and temporal scales of propagation of convection

simulation with Kuo convection during August–September 2.5 mm day^{-1} less compared to the control and closer to the observed value (Fig. 2d, j). However, note that these simulations show a substantial increase in precipitation over the Indian region from June–July to August–September even without orography. Overall, these results show that removal of orography reduces the monsoon precipitation substantially during the first half of the monsoon season (June–July). However, orography does not have a large impact on the intensity of monthly mean precipitation during the later half of the season (August–September), i.e., in the post-onset phase. Similar reduction in monsoon

precipitation during June–July was noticed when orography was removed only over the Asian continent (not shown). The ensemble mean results from SAS and Kuo cumulus convections for control and *noGlOrog* simulations shown above were very similar to that from individual members. Using a student's *t* test, we have found that these differences between control and *noGlOrog* simulations in ensemble mean precipitation during June–July averaged over the Indian region were significant at more than 99 % level.

5.1 Intraseasonal variation

Time series of daily precipitation over the Indian region from TRMM estimates, and ensemble mean control and *noGlOrog* simulations of the model are shown in subpanels a and b of Fig. 3 for SAS and Kuo cumulus convections, respectively. Note that the rate of daily precipitation was similar in the TRMM data sets and control simulation of the model with SAS cumulus convection. If all-India precipitation onset date (this date could be different from onset over Kerala) is defined as the day when all India daily mean precipitation exceeds 4 mm day^{-1} and stays above this value for at least five consecutive days (Chakraborty et al. 2006), then the onset date in the TRMM data set was 18 June and in control simulation with SAS convection the onset date was 6 June. Figure 3a shows that daily precipitation rate from *noGlOrog* simulation was mostly around 1–2 mm day^{-1} up to 15 July, after which it increased sharply. Using the same definition of onset date, it was found that in *noGlOrog* simulation with SAS cumulus convection the onset date was 18 July, 42 days later than the control run.

The basic characteristics of daily precipitation over this region remains unchanged when Kuo convection was used. Fig. 3b shows the results with Kuo cumulus convection. Monsoon onset was in the beginning of June with orography (5 June) and was delayed by about 44 days in its absence (19 July). However, Kuo convection produces more variation in daily precipitation compared to the SAS convection (Fig. 3a, b).

It was found that the standard deviation of onset dates between individual members were much smaller compared to the difference in (ensemble mean) onset dates between the control and *noGlOrog* simulations. For example, the standard deviation of onset dates between control *(noGlOrog)* members for SAS convection was 8.4 days (18.9 days). These values were much smaller compared to the difference in ensemble mean onset dates between these two experiments (42 days). Therefore, it can be stated that these differences in onset dates between control and *noGlOrog* simulations are statistically significant.

This delay in onset without orography was due to the delay in northward propagation of convection north of 13° N over the Indian land region as can be seen from

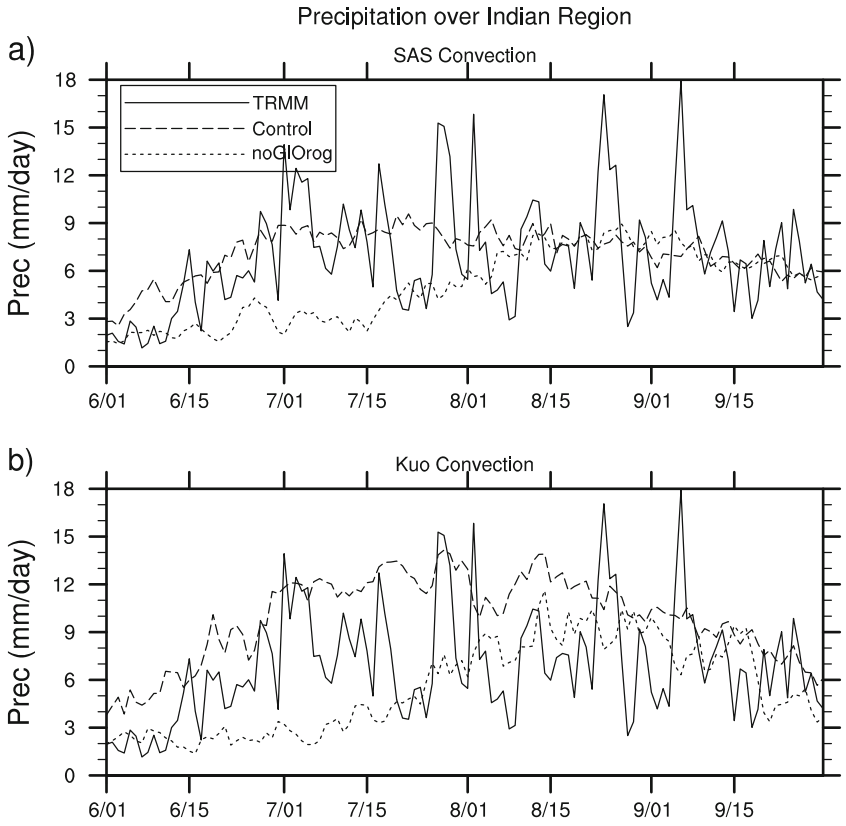

Fig. 3 Time series of daily precipitation rate over the Indian region (70−90° E, 8°−28° N) from TRMM estimates, and control and *noGlOrog* simulations using (*top*) SAS and (*bottom*) Kuo convection schemes

Figs. 4 and 5. These figures show the time–latitude cross section of precipitation averaged over 75°− 80° E (along the center of Indian land) from TRMM estimates, and model simulation with and without orography using SAS and Kuo cumulus convections, respectively. In general, the model could simulate northward propagation of convection over this longitude belt albeit the phase in the model was not same as that in the TRMM data set. Another major difference between model and observation was that model showed more frequent low-intensity precipitation (2–6 mm day^{-1}) as compared to TRMM estimates. Note that this kind of low intensity precipitation in model is common (e.g., Chakraborty 2010) owing to the fact that the convection scheme generally smoothen subgrid scale precipitation over the larger scale grid.

Convection reached north of 20° N during the middle of June in control simulation (Figs. 4b and 5b). This was similar to that observed in the TRMM data sets (Figs. 4a and 5a). However, for *noGlOrog* simulations, propagating convective system did not cross 15° N latitude until the beginning of July with SAS convection and middle of July with Kuo convection schemes. This delay was responsible for the delay in onset over the Indian region without orography. After the onset phase, the convective systems propagated all the way up to 25° N from near the Equator irrespective of the presence of orography (Figs. 4c and 5c). These results confirm that global orography has a major role to play during the onset of summer monsoon over the Indian region. However, after the onset, precipitation is independent of the presence of orography.

The above analysis gives only a qualitative picture of the change in the intraseasonal pattern. We use wavelet analysis to obtain a quantitative view of the temporal and spatial scales associated with these propagating systems and the impact of orography on intraseasonal variations.

5.2 Spatial scales of northward propagation of convection

Northward propagation of convection systems in the model with and without orography was studied over the longitude band 75°–80° using wavelet analysis. From Figs. 4 and 5, we know that the reduction in precipitation in *noGlOrog* simulation over the Indian region during June and July was due to the lack of northward propagating systems penetrating

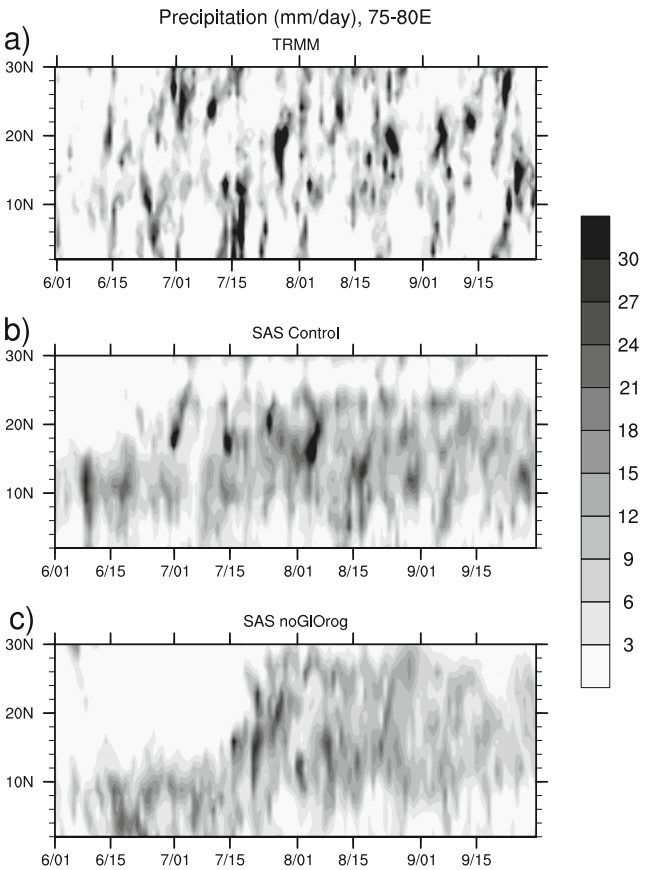

Fig. 4 Northward propagation of convection over the longitude belt 75°−80° E from TRMM estimates, and control and *noGlOrog* simulations using SAS convection scheme

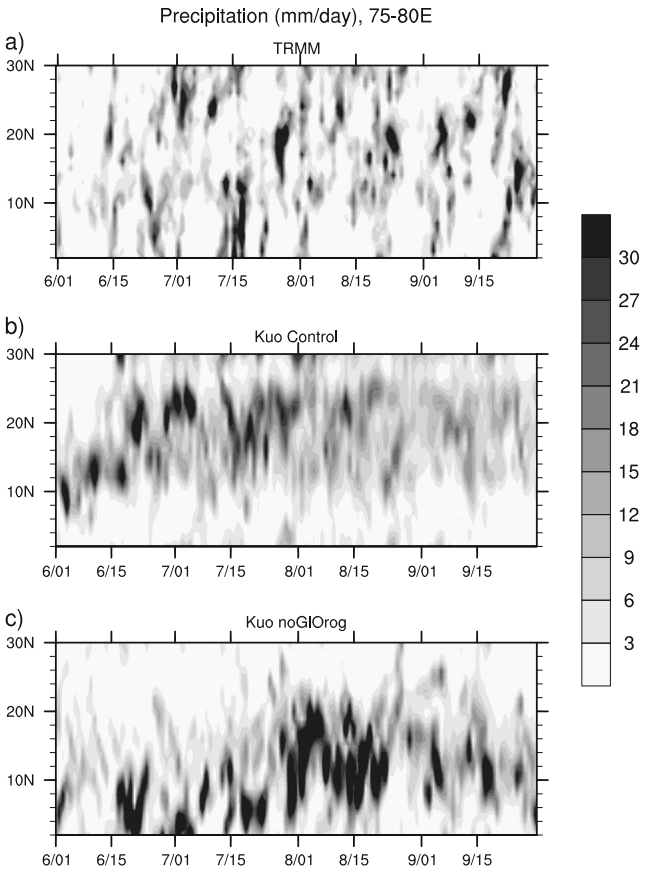

Fig. 5 Northward propagation of convection over the longitude belt 75°−80° E from TRMM estimates, and control and *noGlOrog* simulations using Kuo convection scheme

north of 15° N both for SAS and Kuo convection schemes. Figure 6 shows the time-averaged scalogram along 75°–80° E during the period June–July (top panels) and August–September (bottom panels) from NCMRWF simulations with (left) and without (right) orography. To generate this figure, we have first calculated the two-dimensional (space–time) wavelet spectra for each member of the ensemble and then averaged them. To find robustness of the results, we have also calculated the location of the dominant spatial scale for every member separately. The mean location (in two dimensions) of the of dominant spatial scales of five ensemble members are shown by the "star" symbol on the plot. Also shown, by solid lines around the mean, are the one standard deviations of this location between ensemble members. note that, for five member ensemble (4 *df*), this length is nearly equal to the 95 % confidence band using *t* test. Figure 6 shows that the ensemble mean location of the dominant spatial scales from different members almost coincides with the location of dominant spatial scale found after averaging spectra from individual members. This is possible due to the fact that all the individual members have similar wavelet spectrum. We did not calculate this ensemble mean location of spatial scale for *noGlOrog* simulation during June–July because it was not possible to find the dominant spatial scale for the members due to delay in onset. The COI, beyond which edge effects become important due to the finite length of the data, is shown as solid line. It can be noticed that in control simulation, the dominant spatial scale was 24° along this longitude both during June–July and August–September. However, the center of the dominant spatial scale was shifted southward by about 3° during August–September from its location during June–July (13° N).

For the *noGlOrog* simulation, there was no dominant spatial scale during June–July along 75° – 80° E signifying that there was no meridional propagation. This result was consistent with that shown previously (Fig. 4). During August–September, the 24° spatial scale of propagation was centered at 10° N in this simulation. This shows that meridional propagation was present over this longitude in this period (Fig. 4). Also noticeable is the similarity in the dominant spatial scale (24°) in control and *noGlOrog* simulations after the establishment of monsoon over the Indian region. The spatial scale of northward propagation of convection was independent of orography after the onset.

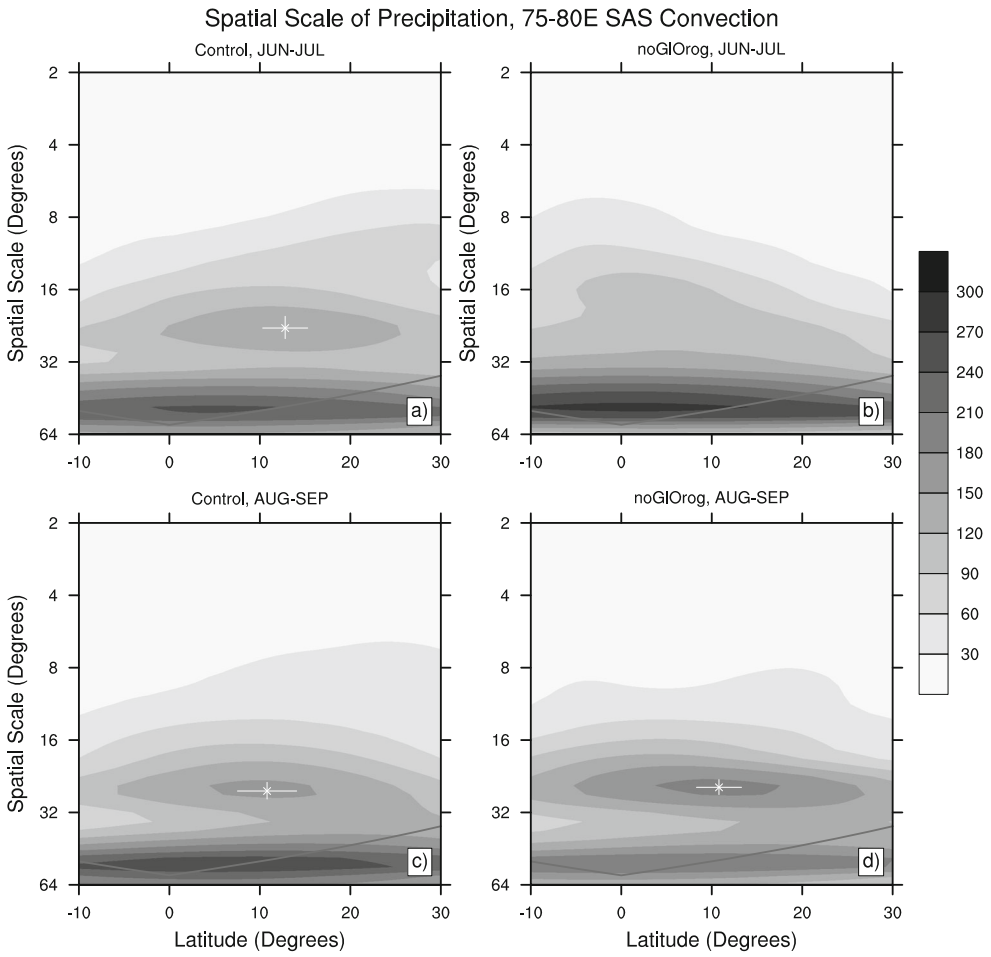

Fig. 6 Time-averaged scalogram for the period June–July (*top*) and August–September (*bottom*) of rainfall data with SAS cumulus convection averaged over the region 75° E–80° E [units (mm day^{-1} degree^{-1})^2]. Also shown is the cone of influence by *solid line*

The results were similar for the Kuo convection scheme (Fig. 7). For the control simulation, the dominant scale was 24° centered at 10° N in June–July. The spatial scale was around 30° centered at 7° N during August–September in the control simulation (Fig. 7c). For the *noGlOrog* simulation, during June–July, the dominant spatial scale was about 18° centered at around 2° N. This shows that there was no northward propagation of convection up to the Indian latitudes during the first half of the monsoon season in absence of orography. During the later half of the season (August–September), the dominant spatial scale appeared to be as 24° for the *noGlOrog* simulation centered north of 11° N. This was consistent with the frequent propagation of convective bands over the Indian region with the removal of orography during this period (August–September) in the model using Kuo convection scheme (Fig. 5).

5.3 Vertical shear of zonal wind

Jiang et al. (2004) have proposed that a presence of strong vertical shear of zonal wind over Indian longitudes can help northward propagation of convection over this region. We have tested this hypothesis in explaining the difference in ISO during early and later parts of the monsoon season in *noGlOrog* experiments. The wind shear is defined as the difference in zonal wind between 200 and 850 hPa. Figure 8 shows zonal wind shear averaged between 70°− 100° E from control and *noGlOrog* experiments during June–July (left panels) and August–September (right panels) both from SAS (top panels) and Kuo (bottom panels) cumulus convection schemes. In June–July with SAS convection scheme (Fig. 8a), magnitude of vertical shear of the zonal wind north of 7° N (Indian latitudes) was 5–15 m s^{-1} lower in *noGlOrog* experiment as compared to control. This weaker shear in *noGlOrog* experiment inhibited northward propagation that was consistent with the delay in monsoon onset over Indian region (Chakraborty et al. 2002). In August–September, magnitude of shear in *noGlOrog* experiments north of 7° N increased and became comparable to the control values (Fig. 8b). However, there was not much change in the value of shear in control simulation from June–July to August–September over Indian latitudes. Similar results are found with Kuo convection scheme (Fig. 8c, d). In June–July, zonal wind shear in

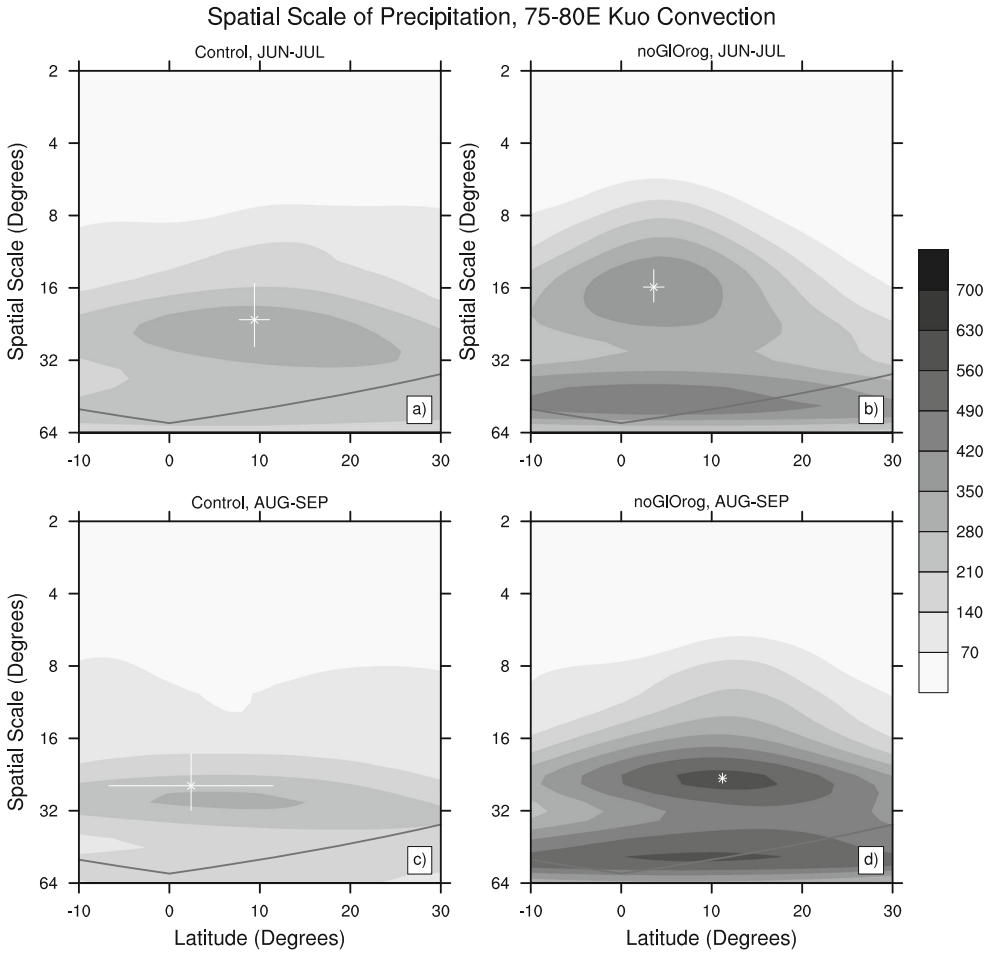

Fig. 7 Time-averaged scalogram for the period June–July (*top*) and August–September (*bottom*) of rainfall data with Kuo cumulus convection averaged over the region 75° E–80° E [units (mm day^{-1} $degree^{-1})^2$]. Also shown is the cone of influence by solid line

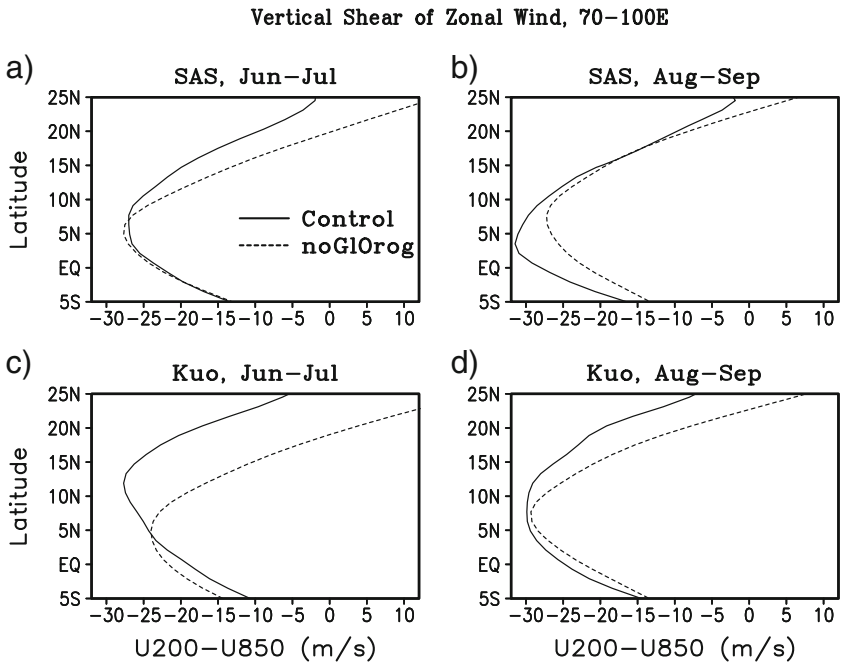

Fig. 8 Vertical shear of zonal wind ($u_{200}-u_{850}$) averaged between 70°−100° E from SAS (*top*) and Kuo (*bottom*) cumulus convection schemes during June–July (*left*) and August–September (*right*)

noGlOrog simulation was much weaker consistent with short spatial scale of northward propagation of convection (Fig. 7). However, in August–September, this vertical shear of zonal wind increases in magnitude that was associated with larger scales of propagation of convective zones over Indian region.

5.4 Temporal scales of northward propagation of convection

Next, we study the temporal evolution of the dominant spatial scales associated with the two cumulus schemes for the ensemble member starting on 1 March 1998. In doing so, the dominant spatial scale (s_x) was chosen from the time-averaged scalogram for each case. Now, the four dimensional field $w(s_x, x, s_t, t)$ of Eq. 6 was averaged over space (x) around the location of maximum power to get a two-dimensional field which is a function of the time scale and time. Hence, this quantity represents the time evolution of dominant spatial scale over the chosen location. Figure 9 shows the time evolution of the dominant spatial scales with and without global orography using SAS cumulus convection (corresponding to Fig. 6). The 24° spatial scale for the control simulation over 15°− 20° N, 75°–80° E was with the time period of 12 days in the beginning of the summer season. The time period increased to about 20 days during second half of June. During July, the power was divided between time period of 10 and 16 days. In August–September over the Indian region, the 24° spatial scale was dominant and the corresponding time period was about 15 days. With the removal of global orography, the convection increased over the Indian region during August–September and the temporal evolution of the dominant spatial scale had a 4-week time period associated with it. Absence of this temporal scale in the early parts of the season resulted in the reduced precipitation over the 70°–90° E, 8°−28° N in the *noGlOrog* simulation.

For Kuo cumulus scheme (Fig. 10), over the Indian region (15°− 20° N, 75°− 80° E), the 24° spatial scale was associated with a time period of around 9 days during late May to late June. After the establishment of monsoon over the Indian region in the middle of June, the time period was found to be around 22 days at this spatial scale.

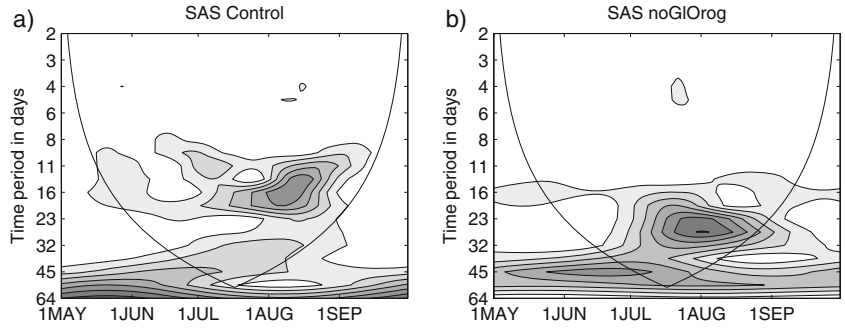

Fig. 9 Evolution of 24° spatial scale over 75°−80° E, 15°−20° N for control and *noGlOrog* experiments during May–September 1998 in the NCMRWF model with SAS cumulus convection. The *left* and *right panels* are in control and *noGlOrog* simulations, respectively. The cone of influence is shown as *solid line*

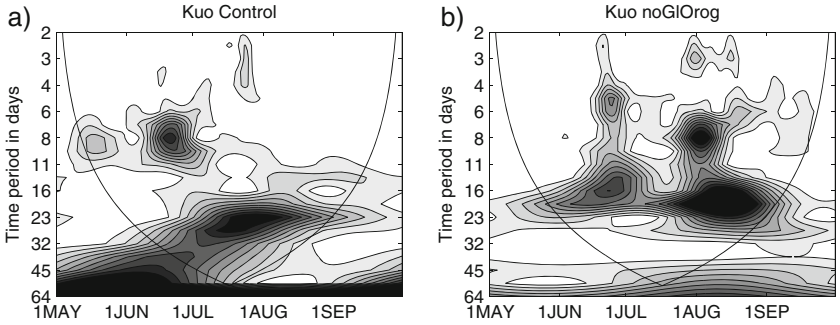

Fig. 10 Evolution of 24° spatial scale over 75°−80° E, 15°−20° N for control and *noGlOrog* experiments during May–September 1998 in the NCMRWF model with Kuo cumulus convection. The *left* and *right panels* are in control and *noGlOrog* simulations, respectively. The cone of influence is shown as solid line

The 24° spatial scale was absent over this region in the *noGlOrog* simulation during the earlier part of the season. It appeared with about 16 days time period in the late June to early July and shifted to about 20 days time period during August. Hence, the absence of 9 and 22 days temporal scale associated with the 24° spatial scale in the early part of the season was responsible for reduction in precipitation over the Indian region with the removal of global orography using Kuo cumulus convection.

5.5 Frequency distribution of precipitation

Precipitation over south Asia occurs in spells of intensity varying from light to heavy. Various factors such as locally generated systems and propagating convective systems of different size and intensity (e.g., land–sea breeze, meridionally/zonally propagating systems, diurnally varying convection) cause variation in rainfall. This variability on the intraseasonal scale contributes to the interannual variation of seasonal mean precipitation. Thus it is necessary to understand the role of orography in modulating the frequency distribution of rainfall rate.

Figure 11 shows histogram of precipitation over south Asian ($60° - 110°$ E, $10°S - 30°$ N) landmass from TRMM observations, and from model simulations with and without mountains (control and *noGlOrog* respectively) using both SAS and Kuo cumulus schemes. Frequency distribution during June–July and August–September are shown separately to understand the differences before and after onset in *noGlOrog* simulations. Distribution from TRMM 3B42 precipitation is shown for June–September combined because we did not find any notable difference in its frequency between June–July and August–September. The first interval (0–0.01 mm day^{-1}) can be considered for "zero-precipitation." This figure suggests that number of grids with zero precipitation is highest in TRMM data over land ($\sim$ 23 %). This value decreases continuously with higher intensity of precipitation. However, the control experiment (open circle) shows higher frequency of precipitation from 3–15 mm day^{-1} range as compared to 0.01–3 mm day^{-1} with SAS convection scheme (Fig. 11) both during June–July and August–September. The *noGlOrog* experiment had most of the grid points ($\sim$ 48 %) with no-precipitation in June–July and the frequency decreases sharply as intensity of precipitation increases, consistent

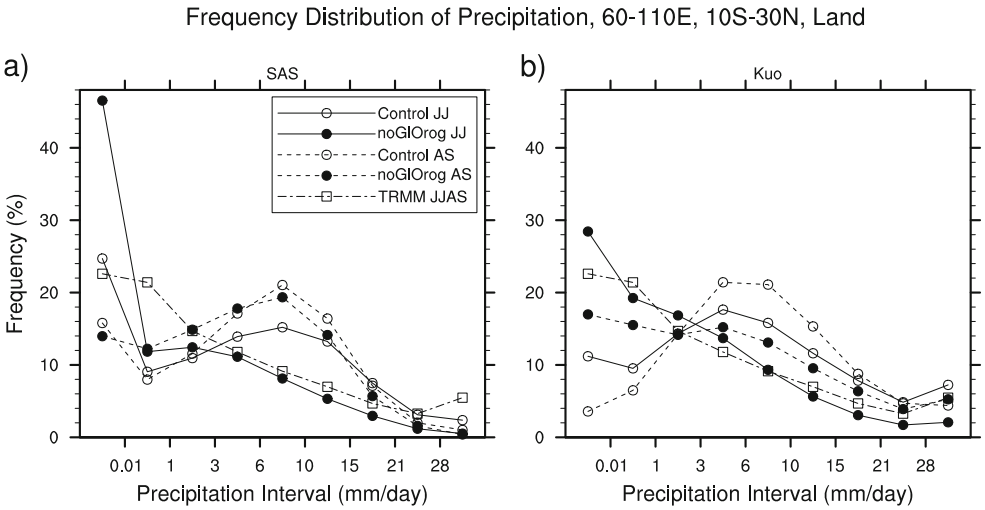

Fig. 11 Frequency distribution of precipitation at different intervals over south Asian land from control (*open circle*) and *noGlOrog* (*filled circle*) experiments during June–July (*solid line*) and August–September (*dashed line*). Corresponding values from TRMM 3B42 data set during June–August 1998 is shown as *open square*

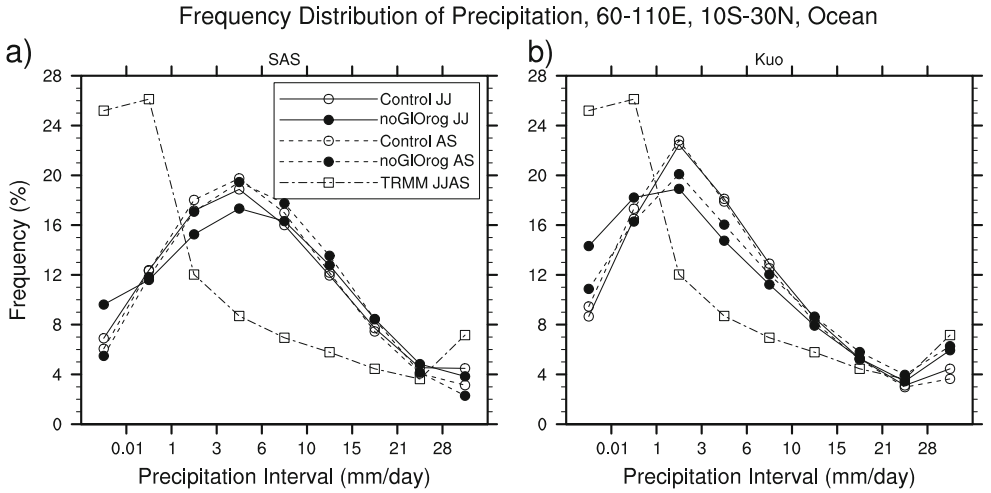

Fig. 12 Frequency distribution of precipitation at different intervals over south Asian ocean from control (*open circle*) and *noGlOrog* (*filled circle*) experiments during June–July (*solid line*) and August–September (*dashed line*). Corresponding values from TRMM 3B42 data set during June–August 1998 is shown as *open square*

with low mean precipitation over this region. However, in August–September, both control and *noGlOrog* experiments show similar frequency distribution. This shows that orography has no impact in determining frequency distribution of precipitation after onset of monsoon with SAS convection scheme.

The control simulation of the model shows higher frequency of precipitation in moderate range (3–10 mm

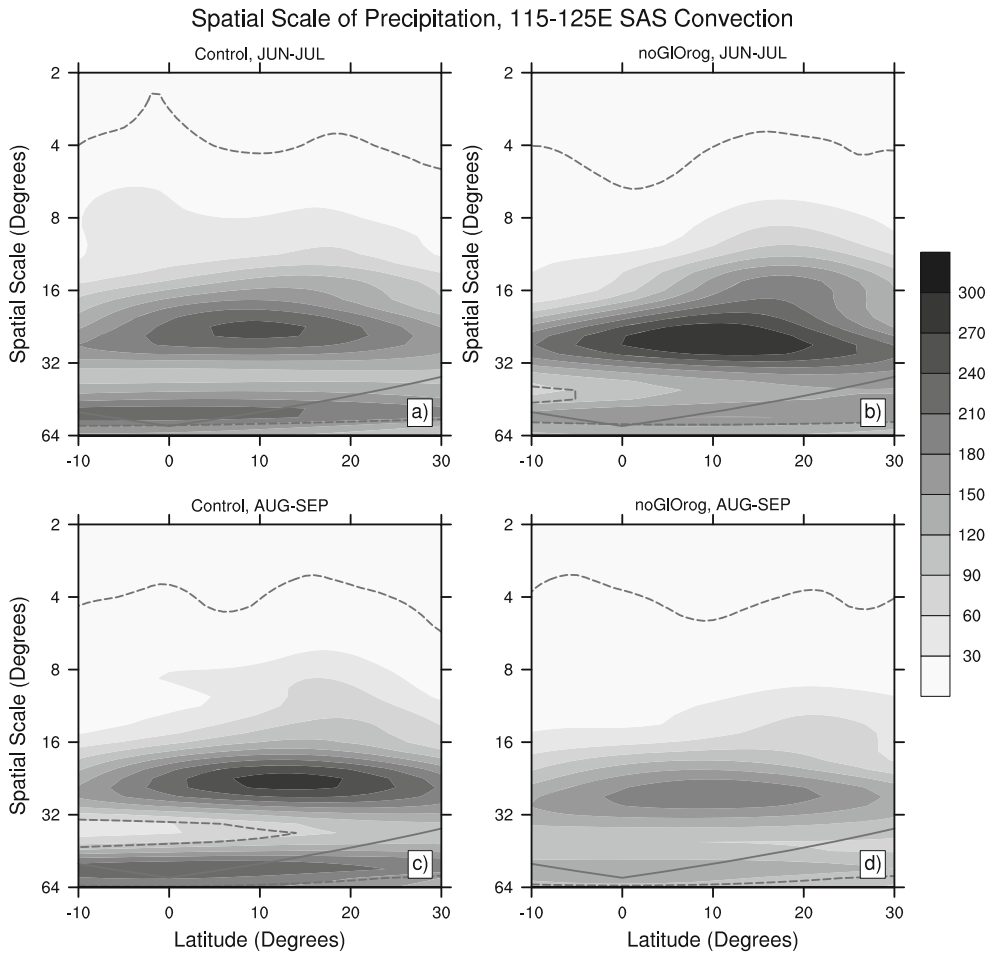

Fig. 13 Time-averaged scalogram for the period June–July (*top panels*) and August–September (*bottom panels*) of precipitation with SAS cumulus convection with (*left panels*) and without (*right panels*) orography averaged over the region 115° E–125° E [units (mm day^{-1} degree^{-1})^2] for the member of the ensemble starting on 1 March 1998. Also shown are the 95 % significance regions by dashed contour and cone of influence by *solid line*

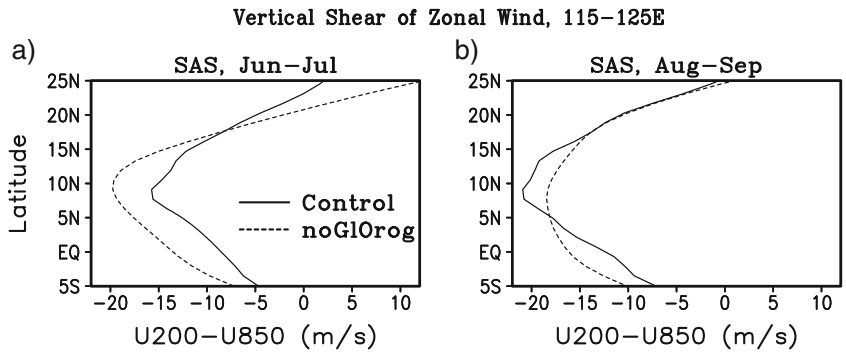

Fig. 14 Vertical shear of zonal wind ($u_{200} - u_{850}$) averaged between 115°−125° E from SAS cumulus convection schemes during June–July (*left*) and August–September (*right*)

day^{-1}) as compared to TRMM estimates in both June–July and August–September. Model simulated frequency in low precipitation ranges ($\leq$ 3 mm day^{-1}), on the other hand, was much smaller as compared to TRMM. This is consistent with earlier findings with ECMWF model that tends to precipitate too much drizzle (Chakraborty 2010). Figure 11b also shows that in *noGlOrog* experiment during August–September, the number of grid points with precipitation higher than 3 mm day^{-1} has increased as compared to its June–July value. However, these frequencies are still smaller than the corresponding August–September value of control experiment. This could be related to the fact the Kuo Scheme is based on low-level convergence and tend to show high precipitation close to regions of orographic uplift.

Figure 12 shows the frequency distribution over the oceanic region around India. Note that the model with both convection schemes tend to underestimate frequency of light precipitation and overestimate frequency of heavy precipitation. However, there was no notable difference in June–July vs August–September distribution of frequencies in either control or *noGlOrog* simulations. The above results suggests that both in SAS and Kuo schemes, frequency distribution of precipitation over south Asia is largely independent of orography after the onset of monsoon. Differences over land part using Kuo schemes could be related to its strong association with upliftment of moisture and precipitation along orographic slopes. It is also interesting to note that the model does not simulate the increase in rainfall at very high intensities ($>$ 28 mm day^{-1}) that is seen in TRMM data both over ocean and land.

5.6 Propagation over West Pacific Ocean

Contrary to the impact of orography over the Indian longitudes, it did not have any impact on northward propagation over the west Pacific Ocean. Time-averaged scalogram along 115°− 125° E for the period June–July and August–September are shown in Fig. 13. The dominant spatial scale in control in June–July was 24° centered at 9° N. The spatial scale remained same during August–September, but the center was shifted to 12° N. Similar to control, in *noGlOrog* simulation, the dominant spatial scale was 24° and centered around the same latitude in June–July. During August–September, in the *noGlOrog* simulation, the scale and center of convective propagation remained unchanged. However, note that the power of propagation in *noGlOrog* experiments was higher during June–July as against August–September. This is consistent with the fact that in *noGlOrog* simulation, west Pacific Ocean was more convectively active in June–July as compared to during August–September, suggesting a seesaw with the Indian region (not shown). These results were similar with Kuo convection scheme as well.

Figure 14 shows vertical shear of zonal wind averaged over 115° − 125° E from control and *noGlOrog* simulations. In June–July, the *noGlOrog* experiment had slightly stronger shear over this region as compared to control. This explains the nearly equal scale of northward propagation in control and *noGlOrog* experiments (Fig. 13a, b). In August–September, both the simulations show very similar shape and intensity of wind shear, consistent again with the similar scale of propagation over this region. These results show that orography does not have large impact on the propagation of convection over west Pacific Ocean either during early or late part of the monsoon season.

6 Conclusions

A large proportion of the interannual variability of summer monsoon over south Asia is associated with meridional propagation of convective zones from near the equator up to the foothills of the Himalayas. It has long been proposed that presence of orography, especially the Tibetan Plateau, determines the observed characteristics of monsoon precipitation over this region. Here, using an atmospheric general

circulation model, we quantify the role of orography on northward propagation of convective zones over south Asia during boreal summer.

Two sets of experiments were performed, one with full orography and another with no orography over the globe. In the full orography experiments, seasonal mean precipitation and its intraseasonal variation was close to the TRMM estimates. However, without orography, the seasonal mean precipitation over the Indian region decreased by about 23 %. These results were significant at more than 99 % level when a t test was used. This decrease was due to a delay in onset of monsoon by about 1 month. This delay in onset was associated with absence of northward propagating convective systems over this region that otherwise brings moisture over the Indian land from equatorial Indian Ocean. We find that occurrence of poleward propagations are related to the meridional variation of vertical shear of the zonal wind. This meridional variation is significantly different during June–July (pre-onset) and August–September periods in the *noGlOrog* simulations.

Two-dimensional (continuous space–time) wavelet analysis were performed to understand and quantify the temporal and spatial scales of these oscillations with and without orography. Our results showed that the dominant spatial scale of propagation along 75°– 80° E was 24° in control simulations during June–July. There was no dominant spatial scale in the no-mountain simulation in this period. Whereas, in August–September, both control and no-mountain simulations showed dominant spatial scale of 24° centered around 10° N. It was found that the absence of 10–30 days time period oscillation over Indian longitude in no-mountain experiment when compared to control was responsible for the reduced rainfall over the Indian region during June–July.

Over West Pacific Ocean (120° E), the dominant spatial scales were found to be 24° in control and no-mountain simulations. This scale did not vary from June–July to August–September in no-mountain experiment, indicating that orography does not have a major role to play in determining northward propagation over west Pacific. Moreover, frequency distribution of precipitation at different intensities are found to be dependent on the convection scheme used in the model. However, orography does not play a major role in determining such distribution after the onset of monsoon.

Our study shows that presence of orography can increase summer monsoon precipitation over Indian region by advancing the date of onset. However, after onset, the basic characteristics of meridionally propagating convective systems and frequency of precipitation at different intensities are largely independent of the presence of orography and are essentially modulated by moist convective processes.

Acknowledgments AC and RSN acknowledge MoES/CTCZ and INCOIS for funding this research. Authors are thankful to Dr Piyush Shankar for discussions.

References

An ZS, Kutzbach JE, Prell WL, Porter SC (2001) Evolution of Asian monsoons and phased uplift of the Himalaya–Tibetan plateau since late Miocene times. Nature 411:62–66

Anthes RA (1977) A cumulus parameterization scheme utilizing a one-dimensional cloud model. Mon Weather Rev 105:270–286

Baliunas S, Frick P, Sokoloff D, Soon W (1997) Time scales and trends in the central england temperature data (1659–1990): a wavelet analysis. Geophys Res Lett 24:1351–1354

Boos WR, Kuang Z (2010) Dominant control of the South Asian monsoon by orographic insulation versus plateau heating. Nature 463:218–222

Broccoli AJ, Manabe S (1992) The effects of orography on midlatitude Northern Hemisphere dry climates. J Climate 5:1181–1201

Chakraborty A (2010) The skill of ECMWF medium range forecasts during the year of tropical convection 2008. Mon Weather Rev 138:3787–3805

Chakraborty A, Nanjundiah RS (2012) Space–time scales of northward propagation of convection during boreal summer. Mon Weather Rev 140:3857–3866

Chakraborty A, Nanjundiah RS, Srinivasan J (2002) Role of Asian and African orography in Indian summer monsoon. Geophys Res Lett 29:522. doi:10.1029/2002GL015

Chakraborty A, Nanjundiah RS, Srinivasan J (2006) Theoretical aspects of the onset of Indian summer monsoon from perturbed orography simulations in a GCM. Ann Geophys 24:2075–2089

Chakraborty A, Nanjundiah RS, Srinivasan J (2009) Impact of African orography and Indian summer monsoon on the low-level Somali Jet. Int J Climatol 29:983–992

Chen L, Reiter ER, Feng Z (1985) The atmospheric heat source over the Tibetan Plateau: May–August 1979. Mon Weather Rev 113:1771–1790

Das S, Mitra AK, Iyengar GR, Mohandas S (2001) Comprehensive test of different cumulus parameterization schemes for the simulation of the Indian summer monsoon. Meteorog Atmos Phys 78:227–244. doi:10.1007/s703-001-8176-1

Das S, Mitra AK, Iyengar GR, Singh J (2002) Skill of medium-range forecasts over the Indian monsoon region using different parameterizations of deep convection. Weather Forecast 17: 1194–1210. doi:10.1175/1520-0434(2002)017<1194:SOMRFO>2.0.CO;2

Daubechies I (1990) The wavelet transform time-frequency localization and signal analysis. IEEE Trans Inform Theory 36:961–1004

Daubechies I (1992) Ten lectures on wavelets. Society for Industrial and Applied Mathematics, Philadelphia, p 355

Farge M (1992) Wavelet transforms and their applications to turbulence. Annu Rev Fluid Mech 24:395–457

Flohn H (1957) Large scale aspects of the summer monsoon in South and East Asia. J Meteorol Soc Jpn 75:180–186

Flohn H (1960) Recent investigation on the mechanism of the summer monsoon of Southern and Eastern Asia. In: Proceedings symposium monsoons of the World. Hind Union, New Delhi, pp 75–88

Flohn H (1968) Contributions to a meteorology of the Tibetan Highland. Atmospheric Science Paper 130, Colorado State University

Foufoula-Georgiou E, Kumar P (eds) (1995) Wavelets in geophysics. Academic Press

Gamage N, Blumen W (1993) Comparative analysis of low-level cold fronts: wavelet, fourier, and empirical orthogonal function decompositions. Mon Weather Rev 121:2867–2878

Grell GA (1993) Prognostic evaluation of assumptions used by cumulus parameterization. Mon Weather Rev 121:764–787

Gu D, Philander SGH (1995) Secular changes of annual and interannual variability in the tropics during the past century. J Climate 8:864–876

Hahn DG, Manabe S (1975) The role of mountains in the south Asian monsoon circulation. J Atmos Sci 32:1515–1541

Hayashi Y (1982) Space–time spectral analysis and its application to atmospheric waves. J Meteorol Soc Jpn 60:156–171

He H, McGinnis JW, Song ZS, Yanai M (1987) Onset of the Asian summer monsoon in 1979 and the effect of the Tibetan Plateau. Mon Weather Rev 115:1966–1994

Jiang X, Li T, Wang B (2004) Structures and mechanism of northward propagating boreal summer intraseasonal oscillation. J Climate 17:1022–1039

Kailas SV, Narasimha R (2000) Quasi cycle in monsoon rainfall by wavelet analysis. Curr Sci 78:592–595

Kitoh A (2004) Effects of mountain uplift on east Asian summer climate investigated by a coupled atmosphere-ocean GCM. J Climate 17:783–802

Krishnamurthy V, Shukla J (2007) Intraseasonal and seasonally persisting patterns of Indian monsoon rainfall. J Climate 20:3–20

Krishnamurti TN, Molinari J, Pan HL (1976) Numerical simulation of the Somali jet. J Atmos Sci 33:2350–2362

Li CF, Yanai M (1996) The onset and interannual variability of the Asian summer monsoon in relation to land–sea thermal contrast. J Climate 9:358–375

Liu PC (1994) Wavelet spectrum analysis and ocean wind waves. In: Foufoula-Georgiou E, Kumar P (eds) Wavelets in geophysics. Academic Press, pp 151–166

Luo H, Yanai M (1983) The large-scale circulation and heat sources over the Tibetan Plateau and surrounding areas during the early summer of 1979. Part I: precipitation and kinematic analysis. Mon Weather Rev 111:922–944

Luo H, Yanai M (1984) The large-scale circulation and heat sources over the Tibetan Plateau and surrounding areas during the early summer of 1979. Part II: heat and moisture budgets. Mon Weather Rev 112:966–989

Manabe S, Broccoli AJ (1990) Mountains and arid climates of middle latitudes. Science 247:192–195

Meyers SD, Kelly BG, O'Brien JJ (1993) An introduction to wavelet analysis in oceanography and meteorology: with application to the dispersion of Yanai waves. Mon Weather Rev 121:2858–2866

Percival DB, Walden AT (2000) Wavelet methods for time series analysis. Cambridge University Press, Cambridge Series In Statistical and Probabilistic Mathematics

Prell WL, Kutzbach JE (1992) Sensitivity of the Indian monsoon to forcing parameters and implications for its evolution. Nature 360:647–652

Prell WL, Kutzbach JE (1997) The impact of Tibet-Himalayan elevation on the sensitivity of the monsoon climate system to changes in solar radiation. In: Ruddiman WF (ed) Tectonic uplift and climate change. Plenum, New York, pp 171–201

Reynolds RW, Smith TM (1994) Improved global sea surface temperature analyses using optimum interpolation. J Climate 7:929–948

Sela JG (1982) The NMC spectral model. NOAA Tech Rep NWS-30:36

Sela JG (1988) The new NMC operational spectral model. Eighth conference on numerical weather prediction. Baltimore, Maryland

Shanker AP, Nanjundiah RS (2004) Morlet wavelet analysis of tropical convection over space and time: study of poleward propagations of Inter Tropical Convergence Zone (ITCZ). Geophys Res Lett 31:150. doi:10.1029/2003GL018

Sikka DR, Gadgil S (1980) On the maximum cloud zone and the ITCZ over Indian longitude during southwest monsoon. Mon Weather Rev 108:1840–1853

Slingo JM, Spencer H, Hoskins B, Berrisford P, Black E (2004) The meteorology of the western Indian Ocean, and the influence of the east African highlands. Phil Trans Royal Soc London 363:25–42

Torrence C, Compo GP (1998) A practical guide to wavelet analysis. Bull of Am Met Soc 79:61–78

Wang B, Wang Y (1996) Temporal structure of the southern oscillation as revealed by waveform and wavelet analysis. J Climate 9:1586–1598

Weng H, Lau KM (1994) Wavelets, period doubling, and time-frequency localization with application to organization of convection over the tropical western pacific. J Atmos Sci 51:2523–2541

Wheeler M, Kiladis GN (1999) Convectively coupled equatorial waves: analysis of clouds and temperature in the wavenumber–frequency domain. J Atmos Sci 56:374–399

Yeh TC (1981) Some characteristics of the summer circulation over the Qighai-Xizang (Tibet) Plateau and its neighborhood. Bull of Am Met Soc 62:14–19